Daniel Voßwinkel, Ulrike Pfannenschmidt, Lukas Heletta, Jasper Arne Baldauf, Theresa Block and Rainer Pöttgen*

Intermetallic phases with $Ho_4Ir_{13}Ge_9$-type structure

https://doi.org/10.1515/znb-2025-0012
Received February 25, 2025; accepted March 20, 2025;
published online May 5, 2025

Abstract: We report on the synthesis an structural characterization of 16 new tetrelides *RE*-(Rh,Ir)-(Si,Ge), the phosphides $Sm_4Rh_{13}P_9$, $Sm_4Ir_{13}P_9$, $Gd_4Ir_{13}P_9$ and $Yb_4Ir_{13}P_9$ and the arsenide $Eu_4Ir_{13}As_9$, which crystallize with the orthorhombic $Ho_4Ir_{13}Ge_9$ type. The structure of $Gd_4Ir_{13}Ge_9$ was refined from single-crystal X-ray diffractometer data: space group *Pmmn*, a = 397.76(2), b = 1,120.97(6), c = 1,935.52(10) pm, w$R2$ = 0.0683, 2,537 F^2 values and 90 refined variables. The iridium and germanium atoms in $Gd_4Ir_{13}Ge_9$ build up a three-dimensional $[Ir_{13}Ge_9]$ polyanionic network which is stabilized by Ir–Ge (240–260 pm) and Ir–Ir (274–294 pm) bonding interactions. The three crystallographically independent gadolinium sites fill large channels within the $[Ir_{13}Ge_9]$ polyanionic network. They have hexagonal prismatic coordination with additional atoms capping the rectangular faces. The structural chemistry of the $Ho_4Ir_{13}Ge_9$ type is compared to the hexagonal phases $RE_4Co_{13}(Si,P)_9$ (*RE* = Sm, Gd–Er), $U_4Fe_{13}P_9$ and the auride $Sr_4In_{13}Au_9$. Magnetic susceptibility data of $Tb_4Ir_{13}Ge_9$ show Curie-Weiss behavior with an experimental magnetic moment of 10.4(1) μ_B Tb atom^{-1}. $Tb_4Ir_{13}Ge_9$ is ordered antiferromagnetically at T_N = 4.7(1) K and undergoes two successive metamagnetic steps.

Keywords: tetrelides; pnictides; metal-rich compounds; intermetallics; magnetic properties

1 Introduction

The rare earth (*RE*) and electron-rich transition (*T*) metals form a large variety of metal-rich phosphides and silicides with a metal:metalloid ratio of close or exactly to 2:1.[1–11] The common structural motif of the many different structure types is the trigonal prismatic coordination of the phosphorus and silicon atoms. Due to the high metal content, these structures contain exclusively *isolated* phosphorus and silicon atoms, i. e., the structures exhibit no P–P or Si–Si bonding. The trigonal prisms are formed by the *RE* and *T* atoms, and they are capped on all rectangular faces, leading to coordination number 9 for the phosphorus and silicon atoms (so-called tri-capped trigonal prisms). The trigonal prisms show condensation via common edges or rectangular faces, leading to characteristic building units. Although this structural description by condensation of trigonal prisms is a purely geometrical one, it is extremely useful to distinguish the individual structure types.

A structure type that belongs to the family of rare earth-rich compounds is $Ho_4Ir_{13}Ge_9$,[12] with the representatives (Table 1) $Ce_4Rh_{13}Ge_9$,[13] $RE_4Ir_{13}Si_9$ (*RE* = Y, Sm, Gd–Lu)[14] and $RE_4Ir_{13}Ge_9$ (*RE* = La–Nd, Sm).[15,16] Interestingly, also the uranium tetrelides $U_4Rh_{13}Si_9$,[17] $U_4Ir_{13}Si_9$ and $U_4Ir_{13}Ge_9$[14] have been synthesized. The complex crystal structures with three crystallographically independent rare earth/uranium sites are associated with interesting magnetic properties. $Gd_4Ir_{13}Si_9$ (T_N = 4.5 K) and $Tb_4Ir_{13}Si_9$ (T_N = 4.3 K) show stable antiferromagnetic ground states and pronounced metamagnetic transitions in their 2 K magnetization isotherms. Susceptibility and specific heat measurements of $U_4Ir_{13}Si_9$ (T_{m1} = 18 and T_{m2} = 6.4 K) and $U_4Ir_{13}Ge_9$ (T_{m1} = 25 and T_{m2} = 7 K)[14] showed two successive magnetic phase transitions, and their gamma values classify them as strongly correlated electron systems. $U_4Rh_{13}Si_9$ is a 30 K antiferromagnet.[17]

In continuation of our systematic phase analytical studies on rhodium- and iridium-rich rare earth tetrelides[18–23] we obtained a series of new $Ho_4Ir_{13}Ge_9$-type phases, completing the $RE_4Rh_{13}Si_9$, $RE_4Rh_{13}Ge_9$ and $RE_4Ir_{13}Ge_9$ series. Bismuth and lead flux growth experiments in the ternary *RE*-*T*-P and *RE*-*T*-As systems[24] afforded the first phosphides and the arsenide $Eu_4Ir_{13}As_9$ (Table 2) with $Ho_4Ir_{13}Ge_9$-type structure, nicely underpinning the close crystal-chemical relationship between the silicides and phosphides. The synthesis conditions and the structural chemistry of these phases are reported herein.

***Corresponding author: Rainer Pöttgen**, Institut für Anorganische und Analytische Chemie, Universität Münster, Corrensstrasse 30, 48149 Münster, Germany, E-mail: pottgen@uni-muenster.de
Daniel Voßwinkel, Ulrike Pfannenschmidt, Lukas Heletta, Jasper Arne Baldauf and Theresa Block, Institut für Anorganische und Analytische Chemie, Universität Münster, Corrensstrasse 30, 48149 Münster, Germany

Table 1: Refined lattice parameters (Guinier powder data) of the tetrelides $RE_4T_{13}X_9$ (T = Rh, Ir; X = Si, Ge). Standard deviations are given in parentheses. The isotypic uranium compounds are listed for comparison.

Compound	*a*/pm	*b*/pm	*c*/pm	*V*/nm^3	Reference
$Tm_4Rh_{13}Si_9$	386.60(10)	1,086.1(2)	1,881.7(4)	0.7901	This work
$Lu_4Rh_{13}Si_9$	384.66(12)	1,086.11(17)	1,881.0(3)	0.7858	This work
$U_4Rh_{13}Si_9$	386.1(1)	1,094.8(2)	1,891.9(3)	0.7997	[17]
$Y_4Rh_{13}Ge_9$	393.47(5)	1,115.85(11)	1,932.74(15)	0.8486	This work
$Ce_4Rh_{13}Ge_9$	398.9(1)	1,125.0(3)	1,944.6(5)	0.8727	[13]
$Pr_4Rh_{13}Ge_9$	397.91(6)	1,124.5(2)	1,948.3(2)	0.8718	This work
$Nd_4Rh_{13}Ge_9$	397.31(7)	1,123.55(13)	1,946.1(2)	0.8687	This work
$Gd_4Rh_{13}Ge_9$	394.80(5)	1,116.46(12)	1,934.06(16)	0.8525	This work
$Tb_4Rh_{13}Ge_9$	393.53(5)	1,116.52(9)	1,933.55(14)	0.8496	This work
$Dy_4Rh_{13}Ge_9$	392.54(7)	1,116.04(18)	1,932.9(3)	0.8468	This work
$Ho_4Rh_{13}Ge_9$	391.79(8)	1,114.95(19)	1,931.2(3)	0.8436	This work
$Er_4Rh_{13}Ge_9$	390.98(8)	1,113.18(17)	1,928.0(3)	0.8391	This work
$Tm_4Rh_{13}Ge_9$	390.43(9)	1,111.1(3)	1,924.6(4)	0.8349	This work
$Y_4Ir_{13}Si_9$	392.5	1,092.2	1,885.6	0.8083	[14]
$Sm_4Ir_{13}Si_9$	395.7	1,101.6	1,898.3	0.8275	[14]
$Gd_4Ir_{13}Si_9$	394.7	1,098.5	1,893.9	0.8211	[14]
$Tb_4Ir_{13}Si_9$	393.6	1,096.1	1,890.8	0.8157	[14]
$Dy_4Ir_{13}Si_9$	392.6	1,094.3	1,887.4	0.8109	[14]
$Ho_4Ir_{13}Si_9$	391.7	1,090.4	1,886.9	0.8059	[14]
$Er_4Ir_{13}Si_9$	391.53(5)	1,091.8(2)	1,884.8(3)	0.8057	[14]
$Tm_4Ir_{13}Si_9$	390.8	1,090.9	1,883.2	0.8029	[14]
$Yb_4Ir_{13}Si_9$	390.6	1,091.6	1,884.9	0.8037	[14]
$Lu_4Ir_{13}Si_9$	389.9	1,091.2	1,880.7	0.8002	[14]
$U_4Ir_{13}Si_9$	389.9(1)	1,095.3(2)	1,892.2(2)	0.8081	[17]
$U_4Ir_{13}Si_9$	390.2	1,092.6	1,894.0	0.8075	[14]
$Y_4Ir_{13}Ge_9$	396.38(4)	1,118.44(14)	1,935.66(19)	0.8581	This work
$La_4Ir_{13}Ge_9$	400.79(5)	1,123.4(4)	1,944.4(8)	0.8755	[15,16]
$Ce_4Ir_{13}Ge_9$	401.08(4)	1,124.1(3)	1,946.6(5)	0.8776	[15,16]
$Pr_4Ir_{13}Ge_9$	401.45(6)	1,124.3(4)	1,946.0(12)	0.8783	[15,16]
$Nd_4Ir_{13}Ge_9$	400.72(5)	1,122.3(3)	1,945.0(5)	0.8747	[15,16]
$Sm_4Ir_{13}Ge_9$	399.22(1)	1,121.70(4)	1,938.35(7)	0.8680	[15,16]
$Sm_4Ir_{13}Ge_9$	397.08(9)	1,122.6(3)	1,944.4(5)	0.8667	This work
$Gd_4Ir_{13}Ge_9$	396.59(7)	1,119.1(2)	1,938.2(3)	0.8602	This work
$Tb_4Ir_{13}Ge_9$	396.60(8)	1,119.0(2)	1,937.3(4)	0.8598	This work
$Dy_4Ir_{13}Ge_9$	395.35(6)	1,118.20(16)	1,935.9(3)	0.8558	This work
$Ho_4Ir_{13}Ge_9$	395.4(3)	1,118.6(3)	1,930.1(6)	0.8537	[12]
$Er_4Ir_{13}Ge_9$	394.44(11)	1,116.3(2)	1,933.3(4)	0.8513	This work
$U_4Ir_{13}Ge_9$	394.7	1,119.8	1,936.1	0.8557	[14]

Table 2: Lattice parameters of phosphides, arsenides, aluminum and indium intermetallics with orthorhombic $Ho_4Rh_{13}Ge_9$-type structure. Standard deviations are given in parentheses.

Compound	Technique	*a*/pm	*b*/pm	*c*/pm	*V*/nm^3	Reference
Phosphides						
$Sm_4Rh_{13}P_9$	Singe crystal	384.79(8)	1,091.6(2)	1,882.4(4)	0.7907	This work
$Sm_4Ir_{13}P_9$	Singe crystal	393.31(8)	1,092.3(2)	1,888.0(4)	0.8111	This work
$Gd_4Ir_{13}P_9$	Singe crystal	392.06(8)	1,090.9(2)	1,883.9(4)	0.8057	This work
$Yb_4Ir_{13}P_9$	Singe crystal	388.31(8)	1,084.7(2)	1,872.8(4)	0.7888	This work
Arsenides						
$Ca_4Rh_{13}As_9$	Singe crystal	390.3(3)	1,122.1(1)	1,941.1(4)	0.8501	[25]
$Sm_4Rh_{13}As_9$	Singe crystal	391.3(3)	1,124.2(6)	1,944.0(6)	0.8552	[25]

Table 2: (continued)

Compound	Technique	*a*/pm	*b*/pm	*c*/pm	*V*/nm^3	Reference
$Eu_4Ir_{13}As_9$	Singe crystal	395.14(4)	1,115.7(1)	1,931.4(3)	0.8515	This work
Aluminum and indium intermetallics						
$Ce_4Al_{13}Pt_9$	Powder	418.26(1)	1,144.24(3)	1,984.75(5)	0.9499	[26]
$Sr_4In_{13}Pt_9$	Powder	439.17(5)	1,232.2(2)	2,135.3(3)	1.1555	[27]

2 Experimental

2.1 Synthesis

Starting materials for the synthesis of the $Ho_4Ir_{13}Ge_9$-type tetrelides and pnictides were ingots of the rare earth elements (Sigma Aldrich, Koch-Light Lab, Smart Elements, ChemPur or Johnson Matthey), rhodium and iridium powder (Agosi), silicon (Smart Elements) and germanium (ChemPur) chips, red phosphorus (Hoechst, Knapsack, ultrapure), bismuth granules (Chempur, 1–10 mm) and lead granules (ABCR GmbH), all with stated purities better than 99.9 %.

The tetrelides were synthesized by arc-melting. The moisture sensitive praseodymium and neodymium pieces were arc-melted to small buttons under an atmosphere of ca. 700 mbar argon (purified using titanium sponge (T = 900 K), silica gel, and molecular sieves). The rhodium and iridium powders were each cold-pressed to pellets of 6 mm diameter. For each sample (ca. 500 mg sample weight), the three elements were weighed in the ideal atomic ratio of 4:13:9 and arc-melted[28] under argon pressure. The product buttons were turned over and remelted several times to ensure sample homogeneity. The weight losses after the diverse melting procedures were all smaller than 1 %. The molten samples were then broken in a steel mortar and part of the product was characterized by its Guinier powder pattern. The remaining parts of the samples were cold-pressed to pellets, re-melted under argon in the arc-melting furnace and sealed in evacuated silica ampoules. The ampoules were heated in a muffle furnace to T = 1,170 K within 2 h. After keeping that temperature for 240 h, the ampoules were quenched in an ice water mixture.

The pnictides were synthesized under metal flux conditions.[29] The phosphides were grown in bismuth fluxes (for a review see ref. 30) with the starting compositions Sm:Rh:P:Bi = 1:2:2:30, Sm:Ir:P:Bi = 1:1:1:30, Gd:Ir:P:Bi = 1.3:2:2:30 and Yb:Ir:P:Bi = 3:1:3:30. The respective elements were weighed in the given atomic ratios and sealed in evacuated silica ampoules. Crystals of $Eu_4Ir_{13}As_9$ were obtained from a starting composition of Eu:Ir:As:Pb = 1:2:2:60 which was placed in an alumina crucible that was subsequently sealed in an evacuated silica ampoule.

The Sm:Rh:P:Bi sample was annealed for 24 h at 770 K in a muffle furnace to pre-react the phosphorus (a too high phosphorus vapor pressure might burst the ampoule). Then it was heated to 1,270 K at a rate of 2 K h^{-1} and kept at that temperature for 168 h. Finally, the sample was cooled at a rate of 2 K h^{-1} to room temperature. The iridium containing samples were also pre-annealed at 770 K, but then heated to 1,370 K at 2 K h^{-1}. After 100 h at 1,370 K, these samples were cooled at a rate of 2 K h^{-1} to 970 K and subsequently at 4 K h^{-1} to 570 K followed by quenching in air. The bismuth and lead fluxes were dissolved in an equimolar mixture of H_2O_2 (ACROS 35 %) and glacial acetic acid (VWR International, >99.8 %). The resulting products were finally rinsed with demineralized water. Besides silvery, rod-shaped crystals of the 4-13-9 phases, by-products were the binary phosphides Ir_2P, IrP_2 and IrP_3.

2.2 X-ray diffraction

The polycrystalline $Ho_4Ir_{13}Ge_9$-type tetrelides were characterized through Guinier powder patterns. The Enraf-Nonius FR552 Guinier camera was operated with Cu$K\alpha_1$ radiation and an image plate detection system (Fujifilm, BAS-1800). α-Quartz (a = 491.30 and c = 540.46 pm) was used as an internal standard. The orthorhombic lattice parameters (Table 1) were obtained from least-squares fits to the experimental 2θ data. The correct indexing of the reflections was ensured through parallel intensity calculations (program Lazy Pulverix[31]). The experimental and simulated powder patterns of $Tb_4Rh_{13}Ge_9$ are presented as an example in Figure 1.

Small single crystals were selected under an optical microscope from the $Gd_4Ir_{13}Ge_9$, $Sm_4Rh_{13}P_9$, $Sm_4Ir_{13}P_9$, $Gd_4Ir_{13}P_9$, $Yb_4Ir_{13}P_9$ and $Eu_4Ir_{13}As_9$ samples. The crystals were fixed to thin glass fibers using beeswax and their quality was first tested by Laue photographs on a Buerger camera (white molybdenum radiation, image plate technique, Fujifilm, BAS-1800). Complete data sets were collected

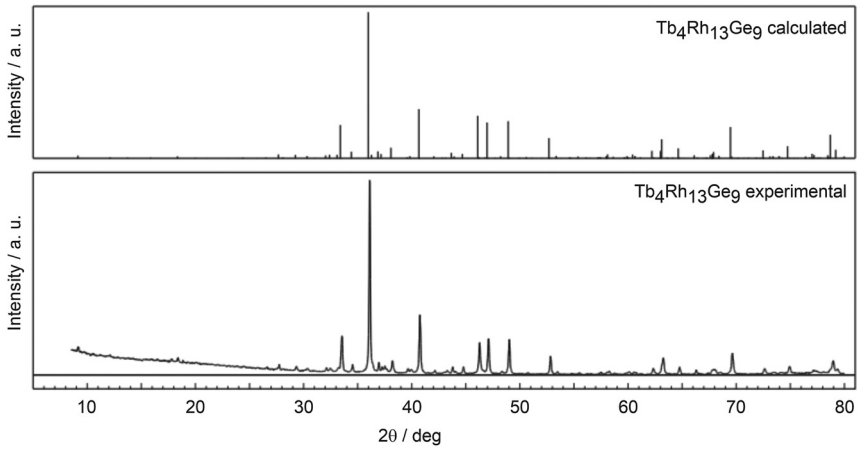

Figure 1: Calculated (top) and experimental (bottom) Guinier powder patterns (Cu$K\alpha_1$ radiation) of the $Tb_4Rh_{13}Ge_9$ sample.

at room temperature on a STOE IPDS-II diffractometer (graphite-monochromatized Mo$K\alpha$ radiation; oscillation mode). Numerical absorption corrections were applied to the data sets. The pnictide data sets showed severe trilling formation and their quality was not sufficient to perform reliable structure refinements. Therefore, only their lattice parameters are listed in Table 2. Details about the data collection and the structure refinement of $Gd_4Ir_{13}Ge_9$ are listed in Table 3.

2.3 EDX analysis

The $Gd_4Ir_{13}Ge_9$ single crystal was analyzed by EDX. The Zeiss EVO® MA10 scanning electron microscope was equipped with a LaB_6 cathode and an Oxford Instruments INCA® x-act detector and operated in variable pressure mode (60 Pa N_2). GdF_3, Ir and Ge were used as standards. The EDX analyses of 14±2 at% Gd: 54±2 at% Ir: 32±2 at% Ge was in fair agreement with the ideal composition (15.4:50:34.6). No impurity elements were detected.

2.4 Magnetic measurements

Magnetic data was measured for the $Tb_4Ir_{13}Ge_9$ sample which was pure on the level of X-ray powder diffraction. A $Tb_4Ir_{13}Ge_9$ piece was attached to the sample holder rod of a Vibrating Sample Magnetometer unit (VSM) using Kapton foil for measuring the magnetization $M(T,H)$ in a Quantum Design Physical Property Measurement System (PPMS). The sample was investigated in the temperature range of 2.5–305 K with applied external magnetic fields up to 80 kOe (1 kOe = 7.96×10^4 A m^{-1}). The data fitting and plotting was performed with OriginPro2017[32] and the graphical editing with the program CorelDraw2024.[33]

3 Structure refinement

The isotypy of $Gd_4Ir_{13}Ge_9$ with the orthorhombic $Ho_4Ir_{13}Ge_9$ type[12] (space group *Pmmn*) was already evident from the

Table 3: Single crystal data and refinement parameters of $Gd_4Ir_{13}Ge_9$ at T = 300 K.

Formula	$Gd_4Ir_{13}Ge_9$
Molar mass/g mol^{-1}	3,781.2
Cell parameters	
a/pm	397.76(2)
b/pm	1,120.97(6)
c/pm	1,935.52(10)
Cell volume/nm^3	V = 0.8630
Crystal system	Orthorhombic
Space group; Z	*Pmmn*; 2
Pearson code	*oP*52
Calc. density/g cm^{-3}	14.55
Crystal size/μm^3	20 × 20 × 180
Diffractometer	STOE IPDS-II
Radiation; wave length/pm	Mo$K\alpha$; 71.073
Transm. ratio (min; max)	0.066; 0.396
Abs. coeff./mm^{-1}	130.2
Detector dist./mm	80
Irradiation time/min	4
ω range; increment/deg	0–180; 1
Integr. param. (A; B; EMS)	12.0; −6.0; 0.030
F(000)/e	3,090
θ range/deg	2–32
hkl range	±5; ±16; ±28
No. refl.	15,555
Independent refl.; R_{int}	2,537; 0.0626
Refl. with $I \geq 3\,\sigma(I)$; R_σ	1,569; 0.0432
Data; ref. parameters	2,537; 90
Goodness-of-fit	1.27
$R1$; w$R2$ ($I \geq 3\,\sigma(I)$)	0.0287; 0.0619
$R1$; w$R2$ (all data)	0.0621; 0.0683
Domain ratio/%	90.9(5):7.4(3):1.7(4)
Extinct. coeff.	172(5)
Largest diff. peak; hole/e $Å^{-3}$	5.16; −6.25

Guinier powder pattern. The standardized atomic parameters of $Ho_4Ir_{13}Ge_9$[12] listed in the Pearson data base[34] were taken as starting values and the structure was refined on F^2 with the JANA2020 software package,[35,36] with anisotropic displacement parameters for all atoms. The data set showed trilling formation. The final refinement was conducted with the twin matrices M1 = (1 0 0, 0 1/2 −3/2, 0 1/2 1/2) and M2 = (1 0 0, 0 1/2 −3/2, 0 −1/2 −1/2) and smoothly converged to the residuals and domain ratios listed in Table 3. The final difference Fourier synthesis was contourless. Further details on the refinement, the positional and the displacement parameters and the interatomic distances are listed in Tables 3–5.

CCDC 2425314 contains the supplementary crystallographic data for this paper. These data can be obtained free of charge from The Cambridge Crystallographic Data Centre via www.ccdc.cam.ac.uk/data_request/cif.

4 Crystal chemistry

Detailed phase analytical studies in the ternary systems *RE*-(Rh,Ir)-(Si,Ge) led to 16 new tetrelides with orthorhombic $Ho_4Ir_{13}Ge_9$-type[12] structure (space group *Pmmn*). Parallel work in the respective pnictide systems furthermore revealed the phosphides $Sm_4Rh_{13}P_9$, $Sm_4Ir_{13}P_9$, $Gd_4Ir_{13}P_9$ and $Yb_4Ir_{13}P_9$ and the arsenide $Eu_4Ir_{13}As_9$. All these phases have the Pearson symbol *oP*52 and the Wyckoff sequence $e^9b^3a^5$.

The cell volumes of the $RE_4(Rh,Ir)_{13}(Si,Ge)_9$ tetrelides reported herein and of those known from literature (Table 1) are plotted in Figure 2 as a function of the sequence of the rare earth elements. Within the four series, the cell volumes decrease with increasing atomic number as expected from the lanthanide contraction. Inspection of the literature data shows that the cell volume reported for $La_4Ir_{13}Ge_9$[16] is doubtful. The reported values of the lattice parameters are even smaller than those reported for $Ce_4Ir_{13}Ge_9$ and $Pr_4Ir_{13}Ge_9$. We have repeated the synthesis of a sample with the starting composition 4La:13Ir:9Ge by arc-melting and subsequent annealing at T = 1,170 K for 240 h. The arc-melted sample was mainly composed of $LaIr_3Ge_2$[16] and a phase with a yet unknown composition. $LaIr_3Ge_2$ disappeared after annealing; however, we got no hint for the expected phase.

The structure of $Gd_4Ir_{13}Ge_9$ was refined from single crystal X-ray diffractometer data and is discussed in the following. Although the $Gd_4Ir_{13}Ge_9$ structure contains 17 crystallographically independent atomic sites and seems complex at first sight, it can easily be described by condensation of germanium centered trigonal prisms $Ge@Gd_4Ir_2$ and $Ge@Gd_2Ir_4$ (Figure 3). These prisms are condensed via common edges within the *bc* plane, forming a chain of condensed *shamrocks*[37] which extends in *b* direction. This building unit is inverted (due to many inversion centers of this centrosymmetric space group, e. g., 0, 0, 1/2 or 0, 1/2, 1/2), and, consequently, we obtain alternating strands of identical composition that are shifted with

Table 4: Atomic coordinates and anisotropic displacement parameters (pm^2) for $Gd_4Ir_{13}Ge_9$ (space group *Pmmn*) at 300 K. The anisotropic displacement factor exponent takes the form: $-2\pi^2[(ha^*)^2U_{11} + \ldots + 2hka^*b^*U_{12}]$. U_{eq} is defined as one third of the trace of the orthogonalized U_{ij} tensor. Standard deviations are given in parentheses. All atoms have x = 1/4. $U_{12} = U_{13} = 0$.

Atom	Wyckoff	y	z	U_{11}	U_{22}	U_{33}	U_{23}	U_{eq}
Gd1	2*a*	1/4	0.01986(8)	94(7)	97(7)	101(6)	0	97(4)
Gd2	4*e*	0.55927(10)	0.70793(5)	96(4)	121(5)	96(4)	−13(4)	105(3)
Gd3	2*b*	3/4	0.52162(8)	97(7)	105(7)	101(6)	0	101(4)
Ir1	4*e*	0.62746(8)	0.35805(4)	81(3)	80(4)	63(3)	3(3)	75(2)
Ir2	4*e*	0.06662(7)	0.16377(4)	78(3)	73(3)	78(3)	−4(3)	76(2)
Ir3	2*a*	1/4	0.72740(6)	83(5)	92(5)	67(4)	0	81(3)
Ir4	2*a*	1/4	0.35819(7)	196(6)	91(5)	88(5)	0	125(3)
Ir5	2*b*	3/4	0.84274(6)	76(5)	79(5)	90(5)	0	82(3)
Ir6	4*e*	0.04942(8)	0.54624(4)	78(3)	95(4)	78(3)	−14(3)	83(2)
Ir7	4*e*	0.55825(8)	0.04026(4)	82(3)	78(3)	70(3)	−5(3)	77(2)
Ir8	4*e*	0.12307(8)	0.85463(4)	76(3)	83(4)	87(3)	7(3)	82(2)
Ge1	2*b*	3/4	0.10104(16)	80(14)	42(13)	84(12)	0	68(8)
Ge2	2*a*	1/4	0.60035(16)	76(14)	65(14)	68(12)	0	70(8)
Ge3	4*e*	0.5696(2)	0.91558(11)	76(9)	88(10)	74(8)	−1(8)	79(5)
Ge4	4*e*	0.6200(2)	0.23090(11)	70(9)	99(10)	84(9)	−9(8)	84(5)
Ge5	2*a*	1/4	0.23374(15)	84(14)	69(13)	70(12)	0	74(8)
Ge6	4*e*	0.0633(2)	0.41868(11)	100(9)	93(9)	72(9)	−6(8)	88(5)

Table 5: Interatomic distances (pm) in the structure of $Gd_4Ir_{13}Ge_9$. Standard deviations are given in parentheses. All distances of the first coordination spheres are listed.

Gd1:	2	Ge1	307.1(3)	Ir2:	1	Ge5	246.2(2)	Ir6:	2	Ge6	245.2(1)	Ge2:	1	Ir3	245.9(3)
	4	Ge3	309.9(2)		1	Ge4	246.3(2)		1	Ge6	247.4(2)		2	Ir6	248.0(2)
	4	Ir7	315.1(1)		2	Ge3	251.3(1)		1	Ge2	248.0(2)		4	Ir1	254.8(1)
	2	Ir5	332.1(2)		1	Ir7	277.0(1)		2	Ir1	285.5(1)		2	Gd3	308.7(3)
	2	Ir2	346.2(2)		2	Ir5	286.3(1)		2	Ir6	289.6(1)	Ge3:	1	Ir7	241.7(2)
	2	Ir7	347.8(1)		2	Ir8	293.3(1)		2	Gd3	327.7(1)		1	Ir8	246.1(2)
	2	Ir8	350.0(2)		2	Gd2	318.3(1)		1	Gd2	335.8(1)		1	Ir5	246.5(2)
Gd2:	2	Ge4	306.5(2)		1	Gd1	346.2(2)		1	Gd3	339.0(1)		2	Ir2	251.3(1)
	2	Ge5	313.1(1)	Ir3:	1	Ge2	245.9(3)	Ir7:	1	Ge3	241.7(2)		2	Ir7	259.6(2)
	2	Ge6	315.6(2)		4	Ge4	259.4(2)		1	Ge1	245.0(2)		2	Gd1	309.9(2)
	2	Ir1	315.7(1)		2	Ir8	284.4(1)		2	Ge3	259.6(2)	Ge4:	1	Ir1	246.2(2)
	2	Ir2	318.3(1)		4	Ir1	292.9(1)		1	Ir2	277.0(1)		1	Ir2	246.3(2)
	2	Ir4	318.8(1)		2	Gd2	348.7(1)		2	Ir7	284.4(1)		2	Ir8	258.8(2)
	1	Ir6	335.8(1)	Ir4:	2	Ge6	239.8(2)		2	Ir8	293.6(1)		2	Ir3	259.4(2)
	1	Ir5	337.3(1)		1	Ge5	240.9(3)		2	Gd1	315.1(1)		1	Ge1	290.5(3)
	1	Ir3	348.7(1)		2	Gd3	306.1(2)		1	Gd1	347.8(1)		1	Ge4	291.4(3)
	1	Ir8	349.9(1)		4	Gd2	318.8(1)	Ir8:	1	Ge3	246.1(2)		2	Gd2	306.5(2)
Gd3:	2	Ir4	306.1(2)	Ir5:	2	Ge3	246.5(2)		2	Ge4	258.8(2)	Ge5:	1	Ir4	240.9(3)
	2	Ge2	308.7(3)		2	Ge5	247.9(2)		2	Ge1	259.2(1)		2	Ir2	246.2(2)
	4	Ge6	311.0(2)		4	Ir2	286.3(1)		1	Ir3	284.4(1)		2	Ir5	247.9(2)
	4	Ir6	327.7(1)		2	Gd1	332.1(2)		1	Ir8	284.6(1)		4	Gd2	313.1(1)
	2	Ir6	339.0(1)		2	Gd2	337.3(1)		2	Ir2	293.3(1)	Ge6:	1	Ir4	239.8(2)
	2	Ir1	345.1(2)						2	Ir7	293.6(1)		1	Ir1	243.9(2)
Ir1:	1	Ge6	243.9(2)						1	Gd2	349.9(1)		2	Ir6	245.2(1)
	1	Ge4	246.2(2)						1	Gd1	350.0(2)		1	Ir6	247.4(2)
	2	Ge2	254.8(1)					Ge1:	2	Ir7	245.0(2)		2	Gd3	311.0(2)
	1	Ir1	274.7(1)						4	Ir8	259.2(1)		2	Gd2	315.6(2)
	2	Ir6	285.5(1)						2	Ge4	290.5(3)				
	2	Ir3	292.9(1)						2	Gd1	307.1(3)				
	2	Gd2	315.7(1)												
	1	Gd3	345.1(2)												

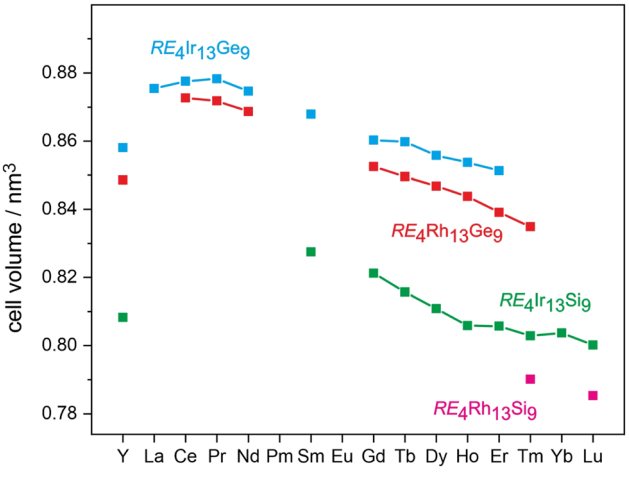

Figure 2: Plot of the cell volumes of the tetrelide series $RE_4T_{13}X_9$ (T = Rh, Ir and X = Si, Ge) with $Ho_4Ir_{13}Ge_9$-type structure. The underlying lattice parameters are summarized in Table 1.

respect to each other by half the translation period a, emphasized by thin and thick lines in Figure 3.

The condensation of the $Ge@Gd_4Ir_2$ and $Ge@Gd_2Ir_4$ prisms leads to the formation of $Ir8_4Ir3_2$ and $Gd2_4Gd3_2$ trigonal prisms at the connection points of the *shamrocks* (shaded in Figure 3). The iridium-based trigonal prisms are too small to be occupied and thus remain empty. Those formed solely by gadolinium atoms are much larger and are filled with the Ir4 atoms. The Ir4 filled $Gd2_4Gd3_2$ trigonal prisms are the structural unit to be noted. These trigonal prisms seem to be too large for the Ir4 atoms and we observe a slightly enhanced U_{11} displacement towards the triangular faces of prisms. This peculiar behavior is most likely a geometrical constraint induced by the prism condensation and a kind of compromise for the $Gd_4Ir_{13}Ge_9$ structure. Many other metal-rich structures with related *shamrock*-like condensation patterns of trigonal prisms show similar

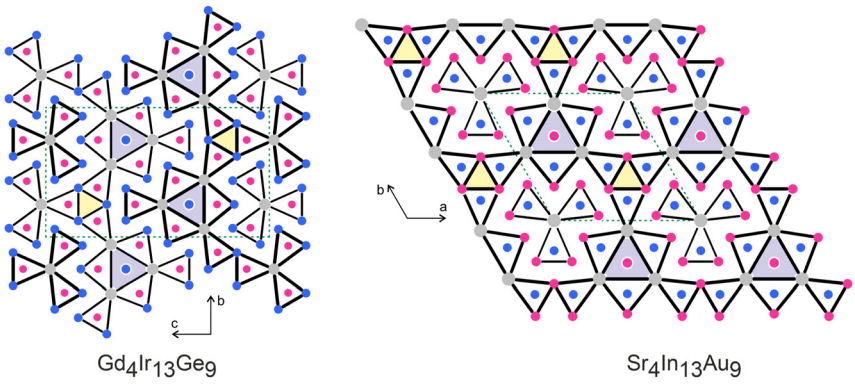

Figure 3: Projection of the $Gd_4Ir_{13}Ge_9$ and $Sr_4In_{13}Au_9$ structures along the short unit cell axes. Gadolinium (strontium), iridium (gold) and germanium (indium) atoms are drawn as medium grey, blue and magenta circles, respectively. All atoms lie on different mirror planes (x = 1/4 and 3/4 for $Gd_4Ir_{13}Ge_9$ and z = 0 and 1/2 for $Sr_4In_{13}Au_9$), accentuated by thin and thick lines. The trigonal prisms around the germanium (gold) atoms are emphasized. The empty Ir_6 (In_6) and filled Ir@Gd_6 (In@Sr_6) prisms are shaded.

displacements of the transition metal atoms with RE_6 trigonal prisms. Typical examples are isotypic $Er_4Ir_{13}Si_9$[14] or the phosphides $Ce_{13}Ir_{34.4}P_{24}$[38] and $Y_7Ir_{17}P_{12}$.[39]

The description of the $Gd_4Ir_{13}Ge_9$ structure with a condensation pattern of trigonal prisms is a purely geometrical one, however, this motif of prism condensation helps to distinguish the many related structure types of metal-rich tetrelides and pnictides. Compilations of such structure types based on the prismatic motifs are given in several overviews.[2–11,40]

The shortest interatomic distances in the $Gd_4Ir_{13}Ge_9$ structure are found between the iridium and germanium atoms. The Ir–Ge distances range from 240 to 260 pm, comparable to the sum of the covalent radii[41] of 248 pm for Ir + Ge. Similar distances have been observed for CeIrGe[42] (256–275 pm Ir–Ge) and $Ce_9Ir_{37}Ge_{25}$[43] (239–262 pm Ir–Ge). Each iridium atom in the $Gd_4Ir_{13}Ge_9$ structure has between three and five germanium neighbors, and both atom types build up a three-dimensional $[Ir_{13}Ge_9]^{\delta-}$ polyanionic network (Figure 4). The three crystallographically independent gadolinium atoms fill slightly distorted hexagonal prisms within the $[Ir_{13}Ge_9]^{\delta-}$ network. The rectangular faces of the hexagonal prisms are all capped by iridium and gadolinium atoms at much longer Gd–Ir and Gd–Ge distances. The prisms filled by the Gd2 and Gd3 atoms form a trimeric unit. This leads to the Ir@Gd_6 prism discussed above which shows the slightly enhanced displacement parameter U_{11} for the Ir4 atoms.

The high iridium content in the $Gd_4Ir_{13}Ge_9$ structure (50 at%) naturally leads to a variety of Ir–Ir interactions. The various Ir–Ir distances (except the *isolated* Ir4 atoms discussed above) range from 274–294 pm. The shorter ones are close to the Ir–Ir distance of 272 pm in *fcc* iridium.[44] This is the typical range in iridium-rich tetrelide and pnictide structures. Closely related structures are, e. g., $Ce_9Ir_{37}Ge_{25}$ (275–294 pm Ir–Ir),[43] $Lu_3Ir_7P_5$ (271–301 pm Ir–Ir)[45] or $La_5Ir_{19}P_{12}$ (282–296 pm Ir–Ir).[46] Thus, the $[Ir_{13}Ge_9]^{\delta-}$ network in $Gd_4Ir_{13}Ge_9$ is stabilized by Ir–Ge and Ir–Ir bonding as well.

The germanium atoms are located within their Gd_4Ir_2 and Gd_2Ir_4 trigonal prisms and show no Ge–Ge bonding. As a consequence of the geometrical constraints of the Ge1@Gd_2Ir_4 and Ge4@Gd_2Ir_4 prism condensation forming the empty Ir_6 prism (Figure 3), the Ge1 and Ge4 centers slightly move towards each other. Nevertheless, the resulting Ge1–Ge4 (291 pm) and Ge4–Ge4 (291 pm) distances are both significantly longer than the 245 pm Ge–Ge single bond distance in the diamond-type modification of germanium,[44] and are no bonding contacts.

Finally, we turn towards the known coloring variants of the $Ho_4Ir_{13}Ge_9$-type[12] structure. Tables 1 and 2 list the known representatives of this structure type. In the family of tetrelides, examples are known with the transition metals rhodium and iridium and the tetrels silicon and germanium. A few pnictides have also been synthesized. The phosphides

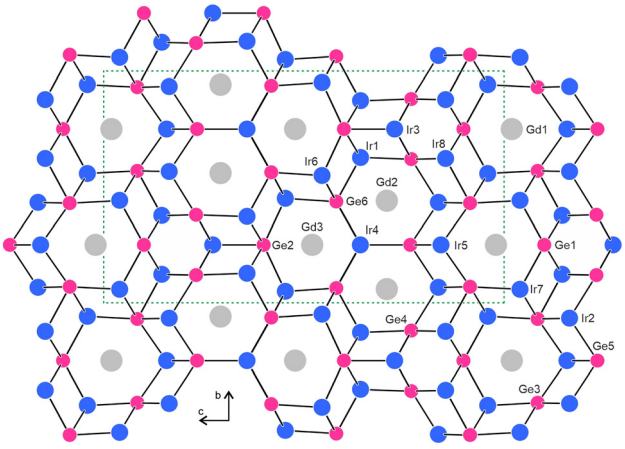

Figure 4: Projection of the $Gd_4Ir_{13}Ge_9$ structure onto the *bc* plane. Gadolinium, iridium and germanium atoms are drawn as medium grey, blue and magenta circles, respectively. The three-dimensional $[Ir_{13}Ge_9]$ network is emphasized. Atom designations are given at the right-hand part of the drawing.

$Sm_4Rh_{13}P_9$ and $RE_4Ir_{13}P_9$ (*RE* = Sm, Gd, Yb) as well as the arsenides $Ca_4Rh_{13}As_9$, $Sm_4Rh_{13}As_9$ and $Eu_4Ir_{13}As_9$ are strictly isotypic with $Ho_4Ir_{13}Ge_9$. Just the tetrel sites are substituted with the pnicogen atoms. This is different for the platinides $Ce_4Al_{13}Pt_9$[26] and $Sr_4In_{13}Pt_9$,[27] which are isopointal[47,48] but not isotypic. The more electronegative platinum atoms occupy the pnicogen sites and thus, this is another example for so-called anti-type structures. The most prominent example concerns the fluorite (CaF_2) and anti-fluorite type (Li_2O). This coloring principle is not that rare in the field of intermetallic compounds. Typical examples are the pairs $Hf_2Co_4P_3$[49] versus $Sr_2In_4Au_3$[50] or $Eu_5In_9Pt_7$[27] versus $Sc_5Pt_9Si_7$,[51] i.e., phosphide versus auride and platinide versus silicide character. The coloring in all these variants is driven by the course of the electronegativities.

A last topic concerns pnictides and an auride that exhibit the same stoichiometry but a different crystal structure. The silicide phosphides $RE_4Co_{13}(Si,P)_9$ (*RE* = Sm, Gd–Er) and $U_4Fe_{13}P_9$[52] and the auride $Sr_4In_{13}Au_9$[53] have a composition similar to $Ho_4Ir_{13}Ge_9$, however, a different connectivity pattern of the trigonal prisms (Figure 3). First, the pair $Ho_4Ir_{13}Ge_9$ versus $Sr_4In_{13}Au_9$ is another example for an electronegativity driven anti-type, similar to the just discussed example. Second, the refined structures of $Gd_4Co_{13}(Si,P)_9$ and $Sr_4In_{13}Au_9$ show slightly enhanced U_{33} displacements for the 1*c* sites (Co in $Gd_4Co_{13}(Si,P)_9$ and In in $Sr_4In_{13}Au_9$). Again, these atoms reside in Gd_6 respectively Sr_6 prisms that are formed as centers of the condensed *shamrock* unit, similar to $Gd_4Ir_{13}Ge_9$, underpinning the close structural relationship.

5 Magnetic properties of $Tb_4Ir_{13}Ge_9$

The temperature dependence of the magnetic susceptibility of $Tb_4Ir_{13}Ge_9$ measured at 10 kOe is presented in Figure 5. $Tb_4Ir_{13}Ge_9$ shows Curie-Weiss behavior above 25 K. A fit of the data (25–300 K range) with a modified Curie-Weiss law yielded an experimental magnetic moment of 10.4(1) μ_B Tb atom^{-1}, a Weiss constant of −6.4(1) K and a temperature-independent contribution of χ_0 = −0.01390(7) emu mol^{-1}. The experimentally derived moment is slightly larger than the free ion value of Tb^{3+} (9.72 μ_B).[54] Such slightly enhanced values have been observed for a variety of intermetallic terbium compounds.[55] The negative Weiss constant is indicative of antiferromagnetic interactions in the paramagnetic range.

The low-field measurement at 100 Oe (insert of Figure 5) clearly reveals antiferromagnetic ordering of the terbium magnetic moments below a Néel temperature of T_N = 4.7(1) K, slightly higher than the one observed for the isotypic silicide $Tb_4Ir_{13}Si_9$ (4.3 K).[14] The magnetization behavior is shown in Figure 6. At 50, 100 and 150 K, well above the magnetic

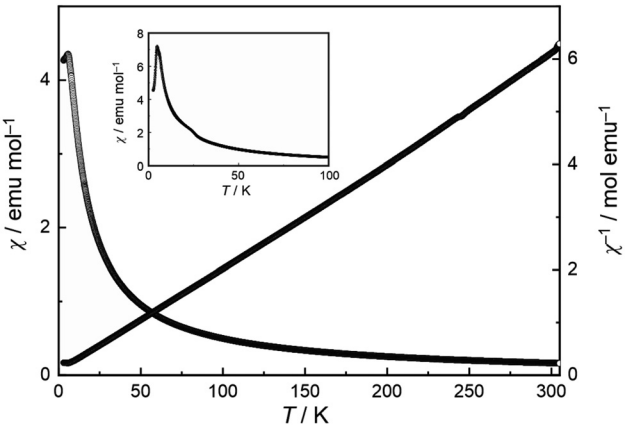

Figure 5: Temperature dependence of the magnetic susceptibility (χ and χ^{-1} values) of $Tb_4Ir_{13}Ge_9$ measured at 10 kOe. The insert shows a 100 Oe measurement that clearly manifests the antiferromagnetic ordering.

ordering temperature, we observe a linear increase of the magnetization with increasing field strength as it is usual for a paramagnetic material. A first curvature occurs in the 10 K isotherm which is still above the Néel temperature. The 3 K isotherm in the magnetically ordered regime shows a two-step metamagnetic behavior (with negligible hysteresis) and thus underpins the antiferromagnetic ground state. The first (poorly pronounced) plateau is around a magnetization of ~2 μ_B per Tb atom. The highest magnetization value at 3 K and 80 kOe of 5.61(1) μ_B per Tb atom is much lower than the theoretical saturation moment of 9 μ_B per Tb atom according to $g_J \times J$.[54] Keeping the three crystallographically independent terbium sites 2*a*, 4*e* and 2*b* in mind, it might be possible, that the first step of the 3 K isotherm corresponds to the antiparallel-to-parallel spin realignment of one of the two-fold sites. This magnetization behavior is similar to that observed

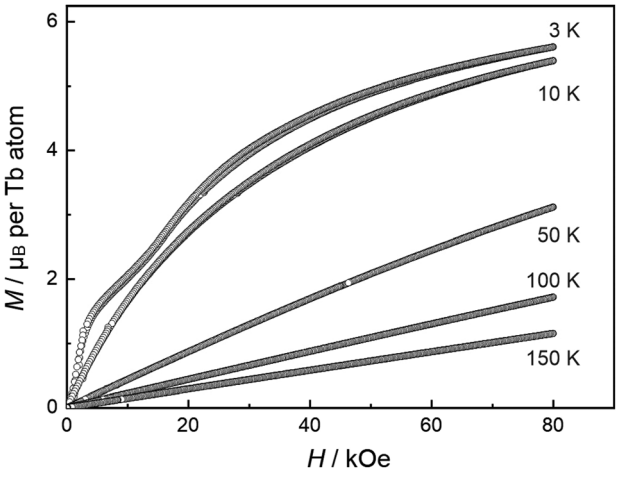

Figure 6: Magnetization isotherms of $Tb_4Ir_{13}Ge_9$ measured at *T* = 3, 10, 50, 100 and 150 K.

for $Tb_4Ir_{13}Si_9$.[14] A quantitative analyses of the terbium spin structure is only possible via neutron diffraction.

Acknowledgements: We thank Dr. R.-D. Hoffmann for the intensity data collection.

Research ethics: Not applicable.

Informed consent: Not applicable.

Author contributions: All authors have accepted responsibility for the entire content of this submitted manuscript and approved the submission.

Use of Large Language Models, AI and Machine Learning Tools: Not relevant. Our group is able to think and act independently.

Conflict of interest statement: The authors declare no conflicts of interest regarding this article.

Research funding: This research was funded by Universität Münster and Deutsche Forschungsgemeinschaft (INST 211/1034-1).

Data availability: Data is available from the corresponding author on well-founded request.

References

1. Parthé, E.; Chabot, B.; Hovestreydt, E. *Acta Crystallogr. B* **1983**, *39*, 596–603.
2. Parthé, E.; Chabot, B. Crystal Structures and Crystal Chemistry of Ternary Rare Earth-Transition Metal Borides, Silicides and Homologues. In *Handbook on the Physics and Chemistry of Rare Earths*. Gschneidner, K. A., Jr., Eyring, L., Eds. Vol. 6; North-Holland: Amsterdam, 1984, pp. 113–332.
3. Parthé, E.; Hovestreydt, E. *J. Less-Common Met.* **1985**, *110*, 307–313.
4. Madar, R.; Ghetta, V.; Dhahri, E.; Chaudouet, P.; Senateur, J. P. *J. Solid State Chem.* **1987**, *66*, 73–85.
5. Pivan, J.-Y.; Guérin, R.; Sergent, M. *J. Solid State Chem.* **1987**, *68*, 11–21.
6. Parthé, E.; Gelato, L.; Chabot, B.; Penzo, M.; Cenzual, K.; Gladyshevskii, R. TYPIX–Standardized Data and Crystal Chemical Characterization of Inorganic Structure Types. In *Gmelin Handbook of Inorganic and Organometallic Chemistry*, 8th ed.; Springer: Berlin, 1993.
7. Kuz'ma, Y.; Chykhrij, S. Phosphides. In *Handbook on the Physics and Chemistry of Rare Earths*, Gschneidner, K. A., Jr., Eyring, L., Eds. Vol. 23, Elsevier Science: Amsterdam, 1996, chapter 156, pp. 285–433.
8. Prots', Yu. M.; Jeitschko, W. *Inorg. Chem.* **1998**, *37*, 5431–5438.
9. Chykhrij, S. I. *Pol. J. Chem.* **1999**, *73*, 1595–1611.
10. Le Sénéchal, C.; Babizhetsky, V. S.; Députier, S.; Pivan, J.-Y.; Guérin, R. *Z. Anorg. Allg. Chem.* **2001**, *627*, 1325–1333.
11. Pöttgen, R.; Hönle, W.; von Schnering, H. G. Phosphides: Solid State Chemistry. In *Encyclopedia of Inorganic Chemistry*, King, R. B., Ed. Vol. VII, 2nd ed., Wiley: New York, 2005, pp. 4255–4308.
12. Sologub, O. L.; Prots, Yu. M.; Salamakha, P. S.; Pecharsky, V. K.; Bodak, O. I. *J. Alloys Compd.* **1993**, *202*, 13–15.
13. Salamakha, P. S.; Sologub, O. L. *J. Alloys Compd.* **1999**, *287*, L1–L3.
14. Vernière, A.; Lejay, P.; Bordet, P.; Chenavas, J.; Tholence, J. L.; Boucherle, J. X.; Keller, N. *J. Alloys Compd.* **1995**, *218*, 197–203.
15. Yarema, M.; Zaremba, O.; Hlukhyy, V.; Fässler, T.; Gladyshevskii, R. *X*th *Intern. Conf. Crystal Chem. Intermetallic Compd.*, Lviv, September 17–20, **2007**, P103.
16. Yarema, M.; Zaremba, O.; Gladyshevskii, R.; Hlukhyy, V.; Fässler, T. F. *J. Solid State Chem.* **2012**, *196*, 72–78.
17. Pikul, A. P.; Kaczorowski, D. *J. Phys. Chem. Solids* **2008**, *69*, 2841–2844.
18. Voßwinkel, D.; Niehaus, O.; Rodewald, U. C.; Pöttgen, R. *Z. Naturforsch.* **2012**, *67b*, 1241–1247.
19. Voßwinkel, D.; Niehaus, O.; Pöttgen, R. *Z. Anorg. Allg. Chem.* **2013**, *639*, 2623–2630.
20. Voßwinkel, D.; Niehaus, O.; Gerke, B.; Benndorf, C.; Eckert, H.; Pöttgen, R. *Z. Anorg. Allg. Chem.* **2015**, *641*, 238–246.
21. Voßwinkel, D.; Matar, S. F.; Pöttgen, R. *Monatsh. Chem.* **2015**, *146*, 1375–1383.
22. Voßwinkel, D.; Benndorf, C.; Eckert, H.; Matar, S. F.; Pöttgen, R. *Z. Kristallogr.* **2016**, *231*, 475–486.
23. Voßwinkel, D.; Pöttgen, R. *Z. Naturforsch.* **2017**, *72b*, 775–780.
24. Pfannenschmidt, U. *Neue übergangsmetallreiche Phosphide und Arsenide der Seltenerdelemente*. Dissertation; Universität Münster: Münster, 2011.
25. Wurth, A.; Keimes, V.; Johrendt, D.; Mewis, A. *Z. Anorg. Allg. Chem.* **2001**, *627*, 2183–2190.
26. Morozova, Y.; Gribanov, A.; Murashova, E.; Dunaev, S.; Grytsiv, A.; Rogl, P.; Giester, G.; Kaczorowski, D. *J. Alloys Compd.* **2018**, *767*, 496–503.
27. Heying, B.; Kösters, J.; Heletta, L.; Klenner, S.; Pöttgen, R. *Monatsh. Chem.* **2019**, *150*, 1163–1173.
28. Pöttgen, R.; Gulden, Th.; Simon, A. *GIT Labor-Fachz.* **1999**, *43*, 133–136.
29. Kanatzidis, M. G.; Pöttgen, R.; Jeitschko, W. *Angew. Chem. Int. Ed.* **2005**, *44*, 6996–7023.
30. Pöttgen, R. *Z. Kristallogr.* **2025**, *240*, 127–139.
31. Yvon, K.; Jeitschko, W.; Parthé, E. *J. Appl. Crystallogr.* **1977**, *10*, 73–74.
32. OriginPro 2024 (version 10.1.0.170), OriginLab Corporation: Nothhampton, Massachusetts (USA), 2024.
33. CorelDRAW Graphics Suite 2017 (version 19.0.0.328), Corel Corporation: Ottawa, Ontario (Canada), 2017.
34. Villars, P.; Cenzual, K.; Eds. *Pearson's Crystal Data: Crystal Structure Database for Inorganic Compounds* (release 2023/24); ASM International®: Materials Park: Ohio (USA), 2023.
35. Petříček, V.; Dušek, M.; Palatinus, L. *Z. Kristallogr.* **2014**, *229*, 345–352.
36. Petříček, V.; Palatinus, L.; Plášil, J.; Dušek, M. *Z. Kristallogr.* **2023**, *238*, 271–282.
37. Zaremba, N.; Krnel, M.; Prots, Y.; König, M.; Akselrud, L.; Grin, Y.; Svanidze, E. *Inorg. Chem.* **2024**, *63*, 4566–4573.
38. Pfannenschmidt, U.; Rodewald, U.Ch.; Pöttgen, R. *Z. Kristallogr.* **2011**, *226*, 229–235.
39. Pfannenschmidt, U.; Pöttgen, R. *Intermetallics* **2011**, *19*, 1052–1058.
40. Gladyshevskii, E. I.; Grin', Y. N. *Sov. Phys. Crystallogr.* **1981**, *26*, 683–689.
41. Emsley, J. *The Elements*; Oxford University Press: Oxford, 1999.
42. Voßwinkel, D.; Block, T.; Pöttgen, R. *Z. Kristallogr. NCS* **2025**, *240*; https://doi.org/10.1515/ncrs-2025-0068.
43. Gaudin, E.; Chevalier, B.; Heying, B.; Rodewald, U. C.; Pöttgen, R. *Chem. Mater.* **2005**, *17*, 2693–2700.
44. Donohue, J. *The Structures of the Elements*; Wiley: New York, 1974.
45. Pfannenschmidt, U.; Rodewald, U. C.; Pöttgen, R. *Z. Anorg. Allg. Chem.* **2010**, *636*, 314–319.
46. Pfannenschmidt, U.; Rodewald, U. C.; Hoffmann, R.-D.; Pöttgen, R. *J. Solid State Chem.* **2011**, *184*, 2731–2737.
47. Gelato, L. M.; Parthé, E. *J. Appl. Crystallogr.* **1987**, *20*, 139–143.
48. Parthé, E.; Gelato, L. M. *Acta Crystallogr.* **1984**, *A40*, 169–183.
49. Ganglberger, E. *Monatsh. Chem.* **1968**, *99*, 566–574.

50. Hoffmann, R.-D.; Pöttgen, R.; Rosenhahn, C.; Mosel, B. D.; Künnen, B.; Kotzyba, G. *J. Solid State Chem.* **1999**, *145*, 283–290.
51. Lorenz, P.; Jung, W. *Z. Anorg. Allg. Chem.* **2009**, *635*, 920–925.
52. Jeitschko, W.; Jakubowski-Ripke, U.; Albering, J. *Z. Anorg. Allg. Chem.* **2011**, *637*, 895–900.
53. Palasyuk, A.; Dai, J.-C.; Corbett, J. D. *Inorg. Chem.* **2008**, *47*, 3128–3134.
54. Lueken, H. *Magnetochemie*; Teubner: Stuttgart, 1999.
55. Szytuła, A.; Leciejewicz, J. *Handbook of Crystal Structures and Magnetic Properties of Rare Earth Intermetallics*; CRC Press: Boca Raton, 1994.